



# Massive Accumulation of Strontium and Barium in Diplonemid Protists

Jana Pilátová,<sup>a,b,c</sup> Daria Tashyreva,<sup>a</sup> Jirí Týč,<sup>a</sup> Marie Vancová,<sup>a,d</sup> Syed Nadeem Hussain Bokhari,<sup>e</sup> Radim Skoupý,<sup>f</sup> Mariana Klementová,<sup>g</sup> Hendrik Küpper,<sup>d,e</sup> Peter Mojžeš,<sup>c</sup> Julius Lukeš<sup>a,d</sup>

<sup>a</sup>Institute of Parasitology, Biology Centre, Czech Academy of Sciences, České Budějovice, Czech Republic

<sup>b</sup>Faculty of Science, Charles University, Prague, Czech Republic

<sup>c</sup>Institute of Physics, Faculty of Mathematics and Physics, Charles University, Prague, Czech Republic

<sup>d</sup>Faculty of Sciences, University of South Bohemia, České Budějovice, Czech Republic

<sup>e</sup>Institute of Plant Molecular Biology, Biology Centre, Czech Academy of Sciences, České Budějovice, Czech Republic

<sup>f</sup>Institute of Scientific Instruments, Czech Academy of Sciences, Brno, Czech Republic

<sup>g</sup>Institute of Physics, Czech Academy of Sciences, Prague, Czech Republic

Jana Pilátová and Daria Tashyreva contributed equally.

**ABSTRACT** Barium and strontium are often used as proxies of marine productivity in palaeoceanographic reconstructions of global climate. However, long-sought biological drivers for such correlations remain unknown. Here, we report that taxa within one of the most abundant groups of marine planktonic protists, diplomemids (Euglenozoa), are potent accumulators of intracellular barite ( $\text{BaSO}_4$ ), celestite ( $\text{SrSO}_4$ ), and strontio-barite ( $\text{Ba,Sr}SO_4$ ). In culture, *Namystinia karyoxenos* accumulates  $\text{Ba}^{2+}$  and  $\text{Sr}^{2+}$  42,000 and 10,000 times higher than the surrounding medium, forming barite and celestite representing 90% of the dry weight, the greatest concentration in biomass known to date. As heterotrophs, diplomemids are not restricted to the photic zone, and they are widespread in the oceans in astonishing abundance and diversity, as their distribution correlates with environmental particulate barite and celestite, prevailing in the mesopelagic zone. We found diplomemid predators, the filter-feeding zooplankton that produces fecal pellets containing the undigested celestite from diplomemids, facilitating its deposition on the seafloor. To the best of our knowledge, evidence for diplomemid biomineralization presents the strongest explanation for the occurrence of particulate barite and celestite in the marine environment. Both structures of the crystals and their variable chemical compositions found in diplomemids fit the properties of environmentally sampled particulate barite and celestite. Finally, we propose that diplomemids, which emerged during the Neoproterozoic era, qualify as impactful players in  $\text{Ba}^{2+}/\text{Sr}^{2+}$  cycling in the ocean that has possibly contributed to sedimentary rock formation over long geological periods.

**IMPORTANCE** We have identified that diplomemids, an abundant group of marine planktonic protists, accumulate conspicuous amounts of  $\text{Sr}^{2+}$  and  $\text{Ba}^{2+}$  in the form of intracellular barite and celestite crystals, in concentrations that greatly exceed those of the most efficient Ba/Sr-accumulating organisms known to date. We propose that diplomemids are potential players in  $\text{Ba}^{2+}/\text{Sr}^{2+}$  cycling in the ocean and have possibly contributed to sedimentary rock formation over long geological periods. These organisms emerged during the Neoproterozoic era (590 to 900 million years ago), prior to known coccolithophore carbonate biomineralization (~200 million years ago). Based on reported data, the distribution of diplomemids in the oceans is correlated with the occurrence of particulate barite and celestite. Finally, diplomemids may provide new insights into the long-questioned biogenic origin of particulate barite and celestite and bring more understanding of the observed

**Editor** L. David Sibley, Washington University School of Medicine

**Copyright** © 2023 Pilátová et al. This is an open-access article distributed under the terms of the [Creative Commons Attribution 4.0 International license](https://creativecommons.org/licenses/by/4.0/).

Address correspondence to Jana Pilátová, jana.pilatova@natur.cuni.cz, Daria Tashyreva, tashyreva@paru.cas.cz, or Julius Lukeš, jula@paru.cas.cz.

The authors declare no conflict of interest.

This article is a direct contribution from Julius Lukeš, a Fellow of the American Academy of Microbiology, who arranged for and secured reviews by Gabriel Gorsky, Laboratoire d'Océanographie Villefranche-sur-Mer, and Virginia Edgcomb, Woods Hole Oceanographic Institution.

**Received** 1 December 2022

**Accepted** 5 December 2022

**Published** 16 January 2023

spatial-temporal correlation of the minerals with marine productivity used in reconstructions of past global climate.

**KEYWORDS** Euglenozoa, barite, biocrystallization, biogeochemical cycles, celestite

Although in most environments strontium (Sr) and barium (Ba) are present in trace amounts, they can be accumulated in substantial quantities by some organisms (1, 2). Depending on their environmental availability, these elements are mostly taken up nonselectively together with  $\text{Ca}^{2+}$  (3, 4). The soluble form of  $\text{Ba}^{2+}$  is typically toxic for animals (e.g., use of rodenticides) due to its capacity to block  $\text{K}^{+}$  channels, while insoluble  $\text{BaSO}_4$  acts as a common contrast agent in medical radio-imaging (5). In contrast, soluble  $\text{Sr}^{2+}$  is not harmful, with the exception of the radioactive isotope  $^{90}\text{Sr}^{2+}$  occurring as a nuclear contaminant that accumulates in marine biota and sediments (6). Indeed, in some algae,  $\text{Sr}^{2+}$  can almost fully replace  $\text{Ca}^{2+}$  without any discernible deleterious effects (7). In humans,  $\text{Sr}^{2+}$  treatment of osteoporosis is used to prevent fractures (8). Moreover, predictions concerning climate change stress the increased relevance of higher environmental mobilization of  $\text{Sr}^{2+}$  and  $\text{Ba}^{2+}$  due to enhanced solubility upon marine acidification (9). Apart from chemical precipitation treatments of radioactive  $^{90}\text{Sr}^{2+}$  and toxic  $\text{Ba}^{2+}$ , there have been new attempts for bioremediation using cyanobacteria, algae, and fungi (1, 2, 6, 10).

In marine environments, microorganisms accumulate more  $\text{Sr}^{2+}$  than  $\text{Ba}^{2+}$ , possibly due to higher solubility and availability, i.e., the concentration of  $\text{Sr}^{2+}$  is around  $88\ \mu\text{M}$  compared to 40 to 150 nM  $\text{Ba}^{2+}$  (11, 12). In protists,  $\text{Sr}^{2+}$  is mostly present in the form of celestite (also referred to as celestine;  $\text{SrSO}_4$ ) and strontianite ( $\text{SrCO}_3$ ), while  $\text{Ba}^{2+}$  forms barite ( $\text{BaSO}_4$ ) or witherite ( $\text{BaCO}_3$ ) (13, 14). Moreover,  $\text{Ba}^{2+}$  and  $\text{Sr}^{2+}$  commonly substitute for each other in various ratios to form strontio-barite and baritocelstite ( $\text{Ba,Sr}(\text{SO}_4)$ ) (15). Celestite with traces of  $\text{Ba}^{2+}$  is well known for forming the complex skeletons of acanthareans (16). Intracellular barite crystals form statoliths of some freshwater charophyte algae and statocysts of marine ciliates, in which they likely play a role in graviperception (13, 17, 18). Haptophytes and foraminiferans form intracellular barite crystals with trace amounts of  $\text{Sr}^{2+}$  (19, 20), while strontianite and witherite occur in microalga *Tetraselmis* (21) and coccolithophorids (14, 22). The exact role of these crystalline inclusions remains unknown.

Marine  $\text{Ba}^{2+}$  and  $\text{Sr}^{2+}$  are frequently correlated with particulate organic carbon in the water column and sediments on the sea floor, indicating that microorganisms are capable of accumulating these elements (11, 23, 24), yet the celestite-rich skeletons of acanthareans dissolve during sedimentation (25).  $\text{Ba}^{2+}$  and  $\text{Sr}^{2+}$  carbonates and phosphates known from coccolithophorids and bacteria, respectively, contribute to the cycling of these elements with possible conversion to sulfates in the process of diagenesis (10, 14, 22, 26). In addition, barite, strontio-barite and celestite crystals are frequently found associated with fecal pellets, which contribute to the sedimentation of particulate  $\text{Ba}^{2+}$  and  $\text{Sr}^{2+}$  to the sea floor (24). However, until now, abundant planktonic organisms capable of selective intracellular accumulation of both  $\text{Ba}^{2+}$  and  $\text{Sr}^{2+}$  sulfates have not been identified (12, 13). The substantial work of Dehairs et al. (24) presents a series of evidence pointing to the biogenic origin of barite/celestite microcrystals, including micrographs of environmental microcrystals covered by desiccated cellular organic matter. Variable composition of marine suspended microcrystalline sulfates are commonly ascribed to barite with minor admixtures of  $\text{Sr}^{2+}$  alongside 10 to 30% of crystals dominated by celestite (24). Such variability is most plausibly explained by active biological catalysis (24). Despite the well-documented evidence-based predictions of the biogenic origins of barite and celestite minerals in the oceans (24, 27), the lack of organisms responsible for their production led to the gradual focus on microenvironment-mediated precipitation, stepping away from consideration of their biological origin (28).

Here, we show that diplonemids (Diplonemea, Euglenozoa), a group of biflagellated heterotrophic protists (29–31), are capable of massive intracellular accumulation of  $\text{Sr}^{2+}$  and  $\text{Ba}^{2+}$ . Specifically, three cultivable diplonemids accumulate celestite and sometimes barite crystals in intracellular concentrations of  $\text{Sr}^{2+}$  much greater than in

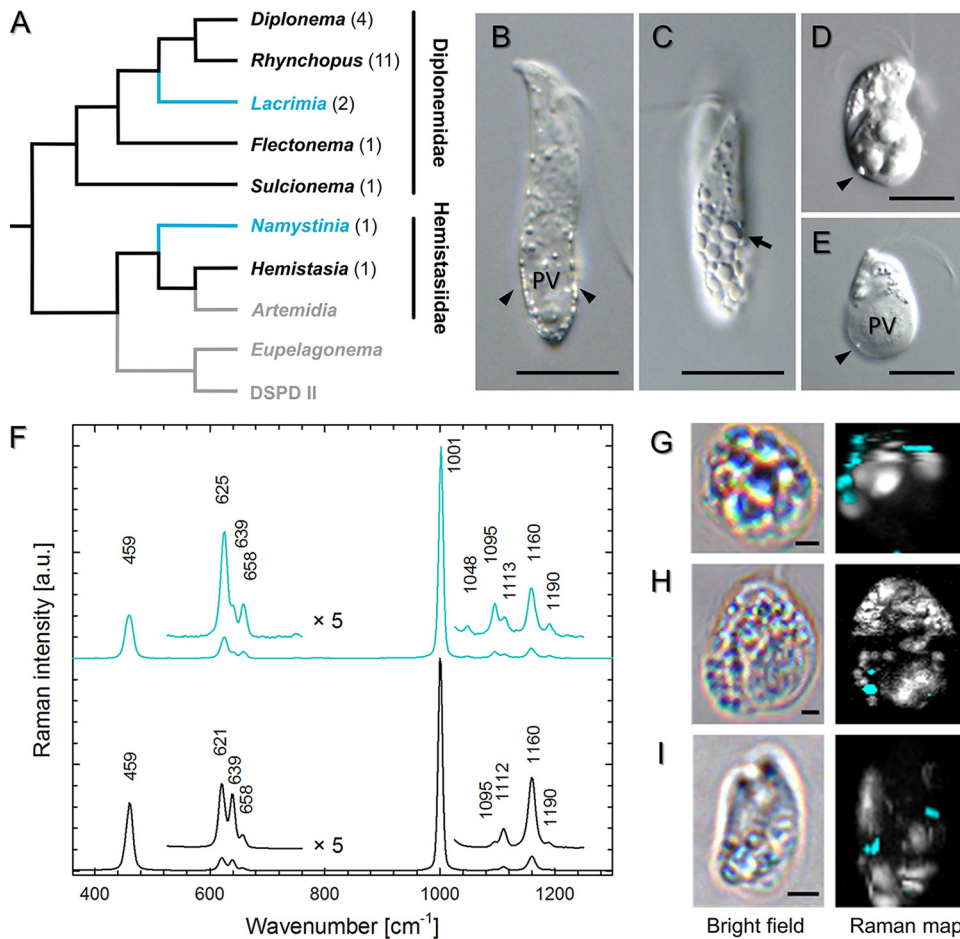


**FIG 1** Distribution of celestite in diplonemids, based on Raman microscopy analysis. (A) Phylogenetic tree of diplonemids based on 29 with genera containing celestite (blue), other screened genera (black), and unexamined clades (gray). (B to E) DIC micrographs of *N. karyoxenos* (B and C), *Lacrimia* sp. YPF1808 (D), and *L. lanifica* (E) with celestite crystals marked by arrowheads; arrow points to a large polygonal crystal. Scale bar, 10  $\mu\text{m}$ . (F) Raman spectra of biogenic celestite crystals found in diplonemid cells (blue) and celestite mineral (black). (G to I) Raman chemical maps of *N. karyoxenos* (G), *Lacrimia* sp. YPF1808 (H), and *L. lanifica* JW1601 (I) with celestite in blue and other cytoplasmic contents in white. Scale bar, 2  $\mu\text{m}$ .

other organisms (10, 19). In the world's oceans, diplonemids have only recently been recognized as omnipresent and one of the most diverse and abundant groups of microeukaryotes (comparable to microalgae), with a prevalence within the mesopelagic protist community (32–34). Although relatively rare, they are present in freshwater bodies as well (35). We analyzed their crystalline inclusions by a range of complementary approaches and discuss here their possible biological functions and role in biogeochemical cycles.

## RESULTS

**Light microscopy and analysis of crystals by Raman microscopy.** To determine the chemical composition of biogenic crystals directly within intact cells, Raman microscopy, a vibrational spectroscopic method sensitive to molecular composition, was used. Out of 21 strains belonging to 15 diplonemid species, three members of the distantly related genera *Lacrimia* and *Namystinia*, represented by *Lacrimia* sp. YPF1808, *Lacrima lanifica*, and *Namystinia karyoxenos*, were shown to possess celestite crystals (Fig. 1A). Their Raman spectra were congruent with the spectra of mineral celestite and chemically prepared precipitates of  $\text{SrSO}_4$  (Fig. 1F), matching also Raman spectra of celestite reported elsewhere (36). Due to the counteraction sensitivity of the position

of the most intense Raman band at around  $1,000\text{ cm}^{-1}$  belonging to the symmetric  $\nu_1$  vibrational mode of the  $\text{SO}_4^{2-}$  tetrahedron, biogenic celestite could be unambiguously identified as  $\text{SrSO}_4$  and was easily distinguishable from barite, baritocelstite, gypsum ( $\text{CaSO}_4$ ), or calcite ( $\text{CaCO}_3$ ) (see Fig. S1 in the supplemental material). Small relative-intensity nuances of other Raman bands of biogenic celestite from various cells (Fig. S2) can be explained by differences in crystal structures (lattice defects), trace admixtures of  $\text{Ba}^{2+}$ , and/or orientations of the crystals, as these are present also in the spectra of mineral reference and chemical precipitates.

When *N. karyoxenos* was examined by light microscopy with differential interference contrast (DIC), the crystalline structures appeared as small birefringent particles moving fast by Brownian motion (Fig. 1B and C; Movie S1). They were most prominent within the enlarged lacunae, which are peripheral membrane-bounded compartments positioned directly beneath the subpellicular microtubular corset (Movie S1), following the addition of 0.1% (wt/vol) formaldehyde. Within a single culture, the size and quantity of crystals inside the cells ranged from a few small particles (Fig. 1B) up to multiple large, tightly packed, polygonal crystals reflecting the shape of orthorhombic prisms (Fig. 1C). The crystalline particles of *Lacrimia* sp. YPF1808 and *L. lanifica* were far less prominent under the light microscope than those of *N. karyoxenos*. However, large crystals were visible around the posterior vacuole with DIC (Fig. 1D and E; Movie S1) and under polarized light (Movie S1).

#### **Morphology, localization, and elemental analysis of intracellular crystals.**

Examination with light, Raman, transmission electron microscopy (TEM), and serial block-face scanning electron microscopy (SBF-SEM) showed that the crystalline inclusions in two clades of diplonemids differed in their localization and shapes. In semithin resin-embedded sections of *N. karyoxenos*, numerous orthorhombic prismatic and bipyramidal crystals were localized mostly inside the lacunae (Fig. 2A, C, and D), with a preference towards the cell posterior. Occasionally, crystals were found inside the large posterior vacuole (Fig. 2A) and in smaller vacuoles scattered throughout the cytoplasm (Fig. 2A and B). Only small crystals could be seen in semithin sections, while bigger crystals dropped out, leaving empty crystal-shaped holes. Due to frequent rupturing, it was not possible to visualize celestite crystals in semithin epoxy resin sections of *Lacrimia* species. Thus, we used the SBF-SEM approach, which showed that the celestite crystals of *Lacrimia* sp. YPF1808 appeared mostly in small membrane-bounded compartments with electron-transparent matrix (Fig. 2H to L) adjacent to the large posterior vacuole (Fig. 2H, I, and K). Three-dimensional (3D) reconstruction revealed that each of these compartments contained one crystal of variable size (Movie S2). Less frequently, crystals were found inside the posterior vacuole (Fig. 2I) or in compartments localized near the anterior flagellar pocket (Movie S2), while they were absent from the cytoplasm and other organelles. The crystals had a shape of rhombic prisms (Fig. 2J and M) or asymmetric tabular prismatic structures with pyramidal and pedial terminations (Fig. 2K and N). Although in *L. lanifica* the celestite crystals were mostly lost from the TEM sections, the positions of holes and ruptures within them and the analysis by Raman microscopy showed similar localizations and sizes of the crystals as those of *Lacrimia* sp. YPF1808 (Fig. 2D, E, H, and I). Likewise, the membrane-bounded compartments were positioned around the posterior vacuole (Fig. 2F), with small asymmetric flattened crystals preserved only occasionally in TEM sections (Fig. 2G).

The presence of celestite crystals (Fig. 1 and 2) was further confirmed by elemental analysis using energy-dispersive X-ray (EDX) spectroscopy in the cryo-SEM-EDX mode of freeze-fractured *Lacrimia* sp. YPF1808 (Fig. 3A and C; Fig. S3) and *N. karyoxenos* cells (Fig. 3B and C; Fig. S4) and by TEM-EDX of whole air-dried cells of *L. lanifica* (Fig. 3E). Atomic percentages estimated by cryo-SEM-EDX analysis were 7.2% Sr and 7.2% sulfur (S), compared to 1.1% Sr and 1.8% S in *Lacrimia* sp. YPF1808 and *N. karyoxenos*, respectively. The dominance of C, N, and O atoms can be explained by the presence of ice and signals from other cellular contents obtained from deeper and/or surrounding areas.

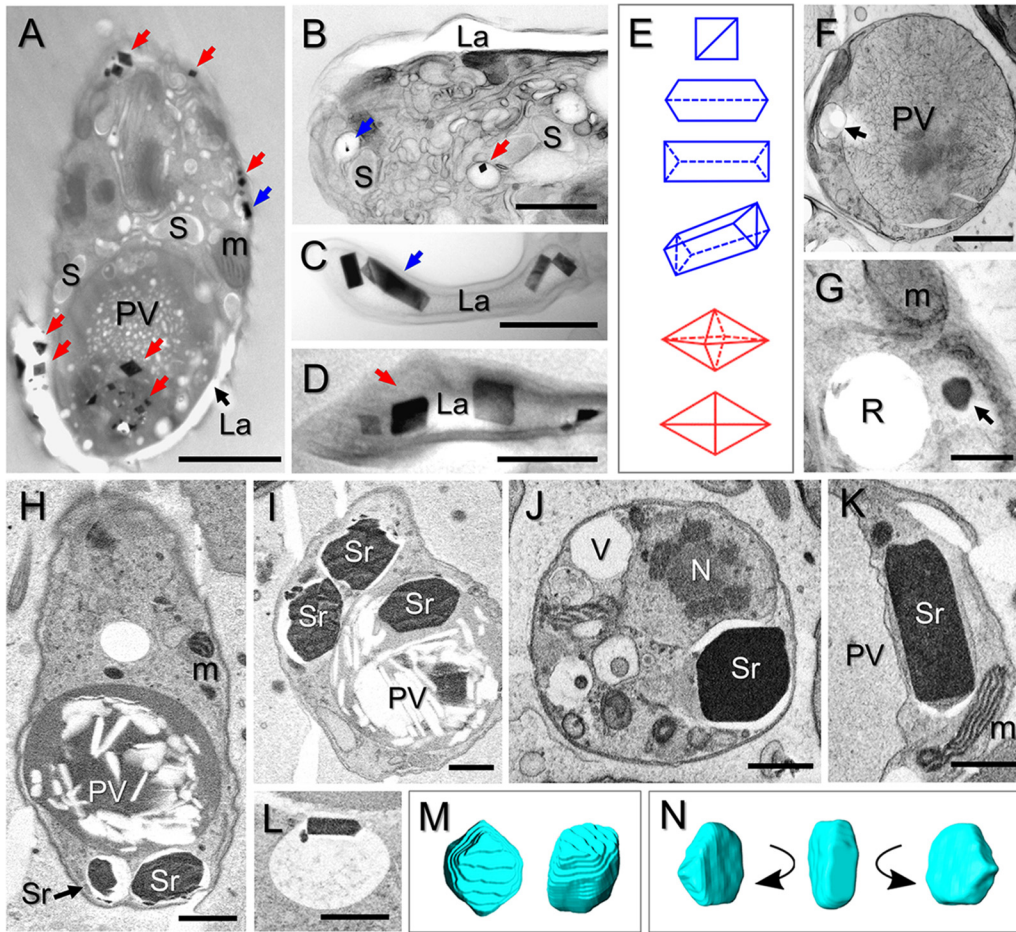


**FIG 2** Crystal structures of naturally occurring celestite with possible barite admixtures in diplonemids. (A to E) TEM images of semithin sections of *N. karyoxenos* with longitudinally sectioned cell showing bipyramidal (red arrows) and prismatic (blue arrow) crystals inside peripheral lacunae and posterior vacuole (A); crystals contained within small vacuoles (B); prismatic (C) and bipyramidal (D) crystals inside lacunae; and a schematic representation of prismatic (blue) and bipyramidal (red) crystals (E). (F and G) TEM images of semithin sections of *L. lanifica* JW1601, with cells cross-sectioned through a posterior vacuole. An arrow points to a small membrane-bounded compartment with the hole left after a dropped-out crystal (F), and another arrow indicates a crystal inside a membrane-bounded compartment and the rupture introduced by a crystal during sectioning (G). (H to L) SBF-SEM images of *Lacrimia* sp. YPF1808 showing celestite crystals inside membrane-bounded compartments and the large posterior vacuole (I). (M and N) 3D reconstructions of celestite correspond to the images in panels J and K, respectively, in shape of rhombic prism (M) or asymmetric tabular prismatic crystal with pyramidal and pedial terminations (N). PV, posterior vacuole; M, mitochondrion; S, endosymbiotic bacteria; La, lacuna lumen; R, rupture; Sr, celestite crystal; N, nucleus. Scale bar, 2  $\mu\text{m}$  (A and F), 1  $\mu\text{m}$  (B and H to K), and 500 nm (C, D, and G).

The identities of celestite crystals in *Lacrimia* sp. YPF1808 (1  $\mu\text{m}$ -thick sections from resin blocks used for SBF-SEM) and *N. karyoxenos* (250 nm-thick resin sections examined by TEM) were confirmed by SEM-EDX and TEM-EDX, respectively (Fig. 3D, F, and G; Fig. S5). Additionally, a significant amount of  $\text{Ba}^{2+}$  was detected in the crystals from *N. karyoxenos*. Crystallographic analysis by electron diffraction showed that the diffraction of measured crystals corresponded to celestite structure (isostructural with  $\text{BaSO}_4$ ) with space group  $Pnma$  and lattice parameters  $a = 8.3 \text{ \AA}$ ,  $b = 5.3 \text{ \AA}$ , and  $c = 6.8 \text{ \AA}$  in *L. lanifica*. Larger lattice parameters ( $a = 8.7 \text{ \AA}$ ,  $b = 5.5 \text{ \AA}$ ,  $c = 7.1 \text{ \AA}$ ) were observed in *N. karyoxenos*, which may be explained by the replacement of  $\text{Sr}^{2+}$  with larger  $\text{Ba}^{2+}$  in the structure of celestite.

**Quantitative analysis by ICP-MS and SBF-SEM.** SBF-SEM-based 3D reconstructions of *Lacrimia* sp. YPF1808 (Movie S2) showed the presence of celestite crystals in all 20 analyzed cells, ranging from 2 to 16 celestite particles per cell (Fig. 4D; Table S2). In total, more than 100 crystals were analyzed, with a volume ranging from 0.017 to

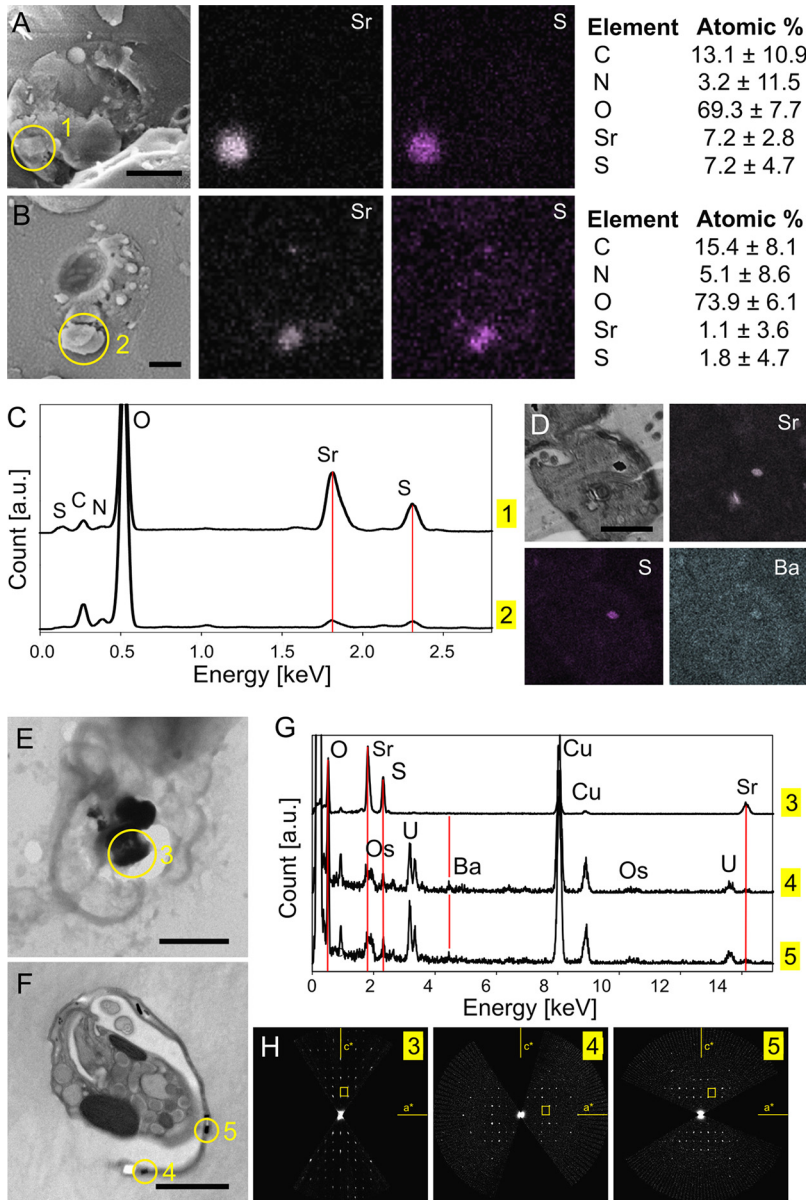


**FIG 3** Elemental analysis of diplonemids. (A to C) Cryo-SEM-EDX images of *Lacrimia* sp. YPF1808 (A) and *N. karyoxenos* (B), complemented with EDX elemental spectral analysis (C) obtained from the area marked by circles 1 and 2, respectively. (D) SEM-EDX images of *Lacrimia* sp. YPF1808 showing the presence of S, Sr, and Ba. (E to G) TEM analysis of celestite microcrystals in a micrograph of a dried cell of *L. lanifica* (E), of a semithin section of *N. karyoxenos* (F), or EDX spectra (G) from the corresponding areas marked 3 to 5, with red lines highlighting the positions of O, Sr, Ba, and S. Cu and C originated from the support grid, and Os and U originated from staining compounds. (H) Electron diffraction for h0l-oriented sections through the 3D ED data sets from the corresponding areas shown in panels E and F. The celestite unit cell is displayed as a yellow rectangle. Scale bar, 2  $\mu\text{m}$ .

7  $\mu\text{m}^3$  (Fig. 4C; Table S2). The impacts of the measured celestite contents on the overall cell density ranged from 0.05% to 9%, with an average of  $1.3 \pm 0.5\%$  (Fig. 4E; Table S2). The calculations were based on the measured volumes, known density of celestite ( $3.9 \text{ g}\cdot\text{cm}^{-3}$ ), and common cellular densities of  $0.985$  to  $1.156 \text{ g}\cdot\text{cm}^{-3}$  reported elsewhere (37).

The lack of celestite crystals in other analyzed species (*Diplonema japonicum*, *Paradiplonema papillatum*, and *Rhynchopus* sp. YZ270) was consistent with the minute  $^{88}\text{Sr}$  content measured by ICP-MS. The high values of  $^{88}\text{Sr}$  in *N. karyoxenos*, *Lacrimia* sp. YPF1808, and *L. lanifica* corresponded to the abundance of intracellular crystals

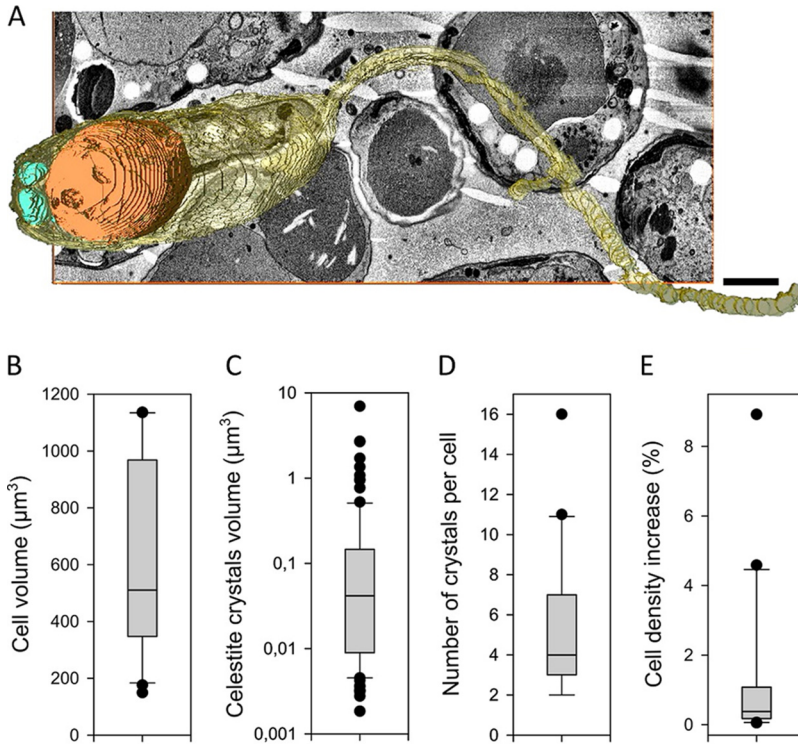


**FIG 4** SBF-SEM images of celestite crystals in *Lacrimia* sp. YPF1808. (A) 3D reconstruction of a cell. Cytoplasm is shown in yellow, large posterior vacuole is in orange, and celestine crystals are in cyan. Scale bar, 1  $\mu\text{m}$ . Descriptive analysis of measured data is for cells ( $n = 20$ ) and crystals ( $n = 106$ ). (B) Distribution of cell volumes. (C) Distribution of celestite crystal volumes on a log scale. (D) Number of celestite crystals per cell. (E) Impacts of celestite crystals on cell density; boxplots show medians and quartiles, and whiskers show the range from minimum to maximum values excluding outliers, represented by single data points.

detected by Raman microscopy, TEM, and SBF-SEM. Since direct measurement of the dry mass was impossible due to the inevitable presence of salts from the medium, the elemental composition analysis by ICP-MS was calculated in atoms per cell or femtomoles per cell. To calculate Sr and Ba content per dry mass, the latter was subsequently estimated by quantitative phase imaging using holographic microscopy (Table 1). The  $^{88}\text{Sr}$  amounts ranged from 0.01  $\text{fmol}\cdot\text{cell}^{-1}$  in *P. papillatum* to  $5,500 \pm 570 \text{ fmol}\cdot\text{cell}^{-1}$  (mean  $\pm$  standard deviation) in *N. karyoxenos*, corresponding to  $340 \pm 38 \text{ mg}\cdot\text{g}^{-1}$ . *Lacrimia* sp. YPF1808 and *L. lanifica* were also potent  $^{88}\text{Sr}$  accumulators, with  $370 \pm 58 \text{ fmol}\cdot\text{cell}^{-1}$  ( $130 \pm 25 \text{ mg}\cdot\text{g}^{-1}$ ) and  $54 \pm 8 \text{ fmol}\cdot\text{cell}^{-1}$  ( $64 \pm 13 \text{ mg}\cdot\text{g}^{-1}$ ), respectively. Depending on the species, the intracellular concentration of  $^{88}\text{Sr}$  was 1,200 to almost 10,000 times higher than in the surrounding medium (Tables 1 and S2).

Compared to the massive accumulation of  $^{88}\text{Sr}$  in diplonemids, the naturally co-occurring Ba was present in much lower amounts (Table 1 and S2), slightly above the detection limit of TEM-EDX analysis (Fig. 3G), possibly reflecting a 12.5 times lower  $\text{Ba}^{2+}$  concentration in the seawater growth medium (Table S1). Nevertheless, the cells concentrated  $\text{Ba}^{2+}$  on average 1,000 to over 42,000 times above the level in the growth medium (Table S1), reaching  $1,200 \pm 130 \text{ fmol}\cdot\text{cell}^{-1}$  ( $120 \pm 14 \text{ mg}\cdot\text{g}^{-1}$ ) in *N. karyoxenos*, with lower values in *Lacrimia* sp. YPF1808 ( $65 \pm 10 \text{ fmol}\cdot\text{cell}^{-1}$ , or  $36 \pm 7 \text{ mg}\cdot\text{g}^{-1}$ ) and *L. lanifica* ( $2 \pm 1 \text{ fmol}\cdot\text{cell}^{-1}$ , or  $4 \pm 1 \text{ mg}\cdot\text{g}^{-1}$ ). Altogether,  $(\text{Ba,Sr})\text{SO}_4$  accumulation reached 91%, 33%, and 14% of dry weight in *N. karyoxenos*, *Lacrimia* sp. YPF1808, and *L. lanifica*, respectively. All strains showed significantly different levels of accumulated Sr or Ba contents (Table 1). Although the concentration of  $\text{Ba}^{2+}$  in our experiment was 30 to 45 times higher than in nature, the stoichiometry per cell was 5 orders of magnitude lower than in the oceans (Table 1).

**Table 1** ICP-MS quantification of <sup>88</sup>Sr and Ba in diplonemids<sup>a</sup>

Species	<i>D. japonicum</i>	<i>P. papillatum</i>	<i>Rhynchopus</i> sp. YZ270	<i>L. lanifica</i> JW1601	<i>Lacrimia</i> sp. YPF1808	<i>N. karyoxenos</i>
Number of cells per ml in culture	2.1·10 <sup>5</sup> ± 9.2·10 <sup>3</sup>	2.2·10 <sup>6</sup> ± 2.1·10 <sup>5</sup>	8.1·10 <sup>5</sup> ± 2.6·10 <sup>4</sup>	7.6·10 <sup>5</sup> ± 2.5·10 <sup>4</sup>	3.7·10 <sup>6</sup> ± 1.7·10 <sup>5</sup>	1.33·10 <sup>6</sup> ± 5.9·10 <sup>4</sup>
Dry weight of cell (pg)	109 ± 2.9	68.0 ± 2.0	74.2 ± 2.7	74.1 ± 3.5	248.1 ± 8.2	1,421 ± 11
Sr (fmol·cell <sup>-1</sup> )	0.22 ± 0.01	0.013 ± 0.001	0.08 ± 0.02	54.4 ± 8.4	366 ± 58	5,530 ± 570
Sr (mg·g <sup>-1</sup> )	0.17 ± 0.10	0.02 ± 0.01	0.10 ± 0.07	64 ± 13	129 ± 25	340 ± 38
<i>p</i>	a	b	a	c	d	e
SrSO <sub>4</sub> (mg·g <sup>-1</sup> )	n/a	n/a	n/a	135	271	715
Concentration of Sr (folds) <sup>a,b</sup>	n/a	n/a	n/a	1,520 ± 680	1,240 ± 550	10,000 ± 3,300
Ba (fmol·cell <sup>-1</sup> )	n/a	n/a	n/a	2.0 ± 0.5	65 ± 10	1,200 ± 130
Ba (mg·g <sup>-1</sup> )	n/a	n/a	n/a	3.7 ± 1.1	35.8 ± 6.8	116 ± 14
<i>p</i>	n/a	n/a	n/a	a	b	c
BaSO <sub>4</sub> (mg·g <sup>-1</sup> )	n/a	n/a	n/a	6.3	61	198
Concentration of Ba (folds) <sup>a,b</sup>	n/a	n/a	n/a	1,130 ± 660	4,300 ± 1,900	42,000 ± 14,000
Total Ba,Sr(SO <sub>4</sub> ) (mg·g <sup>-1</sup> )	n/a	n/a	n/a	141	332	913

<sup>a</sup>The dry weight was measured by quantitative phase imaging (n = 150 cells). Results of ICP-MS are displayed as mean values of biological triplicates with standard error of the mean. All figures are rounded to two significant numbers. The amounts of <sup>88</sup>Sr and Ba per dry mass (mg·g<sup>-1</sup>) was logarithmically transformed and statistically analyzed by one-way ANOVA ( $p < 0.001$  ( $F = 1747.8$  and  $F = 88.6$ ; total degree of freedom:  $df = 17$  and  $df = 8$ , respectively), with Tukey's post-hoc test significant differences on the level  $p < 0.05$  in column *p*).

<sup>b</sup>\*, calculated as atoms·cell<sup>-1</sup> based on analyzed cell pellets relative to the theoretical value in atoms·cell<sup>-1</sup> originating from the culture medium alone (8 mg·l<sup>-1</sup> Sr<sup>2+</sup> and 0.64 mg·l<sup>-1</sup> Ba<sup>2+</sup> – as listed in SI Appendix Table S1); in *N. karyoxenos*, the amount of accumulated Ba exceeds total Ba available per volume of culture medium due to repeated passages of pelleted cells into fresh medium. n/a, not analyzed.

### Ba<sup>2+</sup> loading experiments and elimination of Sr<sup>2+</sup> and Ba<sup>2+</sup> from the medium.

Under our cultivation conditions, Ba<sup>2+</sup> was 20 times less abundant than Sr<sup>2+</sup> (Table S1), which resulted in formation of celestite with Ba<sup>2+</sup> admixtures in the examined species. In oceans, the proportion is even 30 times lower (11, 12). Here, we tested whether increases in Ba<sup>2+</sup> content would impact the biomineralization process by cultivation in artificial seawater loaded with equimolar amounts of Ba<sup>2+</sup> and Sr<sup>2+</sup> to 88 μM. To prevent spontaneous precipitation of barite, we supplemented sulfates with NaCl to maintain the osmolarity of the medium. This resulted in the formation of all mineral combinations: pure barite (Raman marker at 988 cm<sup>-1</sup>), celestite (1,000 cm<sup>-1</sup>), and mixed forms of (Ba,Sr)SO<sub>4</sub> (991 cm<sup>-1</sup>; strontio-barite or baritocelstite) (Fig. 5), revealing that diplonemids do not show a strong preference toward the accumulation of either element.

Both *L. lanifica* and *Lacrimia* sp. YPF1808 contained mostly mixed crystals of (Ba,Sr)SO<sub>4</sub>. In *N. karyoxenos*, pure celestite prevailed in the central part of crystals (999 cm<sup>-1</sup>) while barite dominated at the periphery (988 cm<sup>-1</sup>), and they gradually overlapped each other (Fig. 5C to F). Additionally, after several passages in the artificial medium without Ba<sup>2+</sup> and Sr<sup>2+</sup> (Table S1), barite and celestite were no longer detectable by Raman microscopy. The lack of Ba<sup>2+</sup> and Sr<sup>2+</sup> did not result in altered morphology or growth impairment. We did not observe any Ca<sup>2+</sup>- or Mg<sup>2+</sup>-containing crystals despite high concentrations of both elements in the medium.

**Feeding experiments.** Fecal pellets are an important agent mediating sedimentation of biogenically accumulated minerals to the sea floor: large aggregates of crystals held together by undigested fecal organic matter enable their fast sinking, thus preventing dissolution of micrometer-sized crystals in the water column, which is undersaturated for barite and celestite (15, 24). To experimentally address whether zooplankton feeds on diplonemids and whether their celestite crystals are carried into fecal pellets, we incubated *N. karyoxenos* and *Lacrimia* sp. YPF1808 with freshly captured filter-feeding marine copepods *Centropages typicus*, *Temora longicornis*, and *Acartia* sp., starved for 12 h prior to the experiment. After 5-day cocultivation, we determined by Raman microscopy that the fecal pellets contained copious amounts of celestite derived from diplonemids (Fig. 6B). In the control system of the same population of copepods fed with freshly collected marine plankton, the

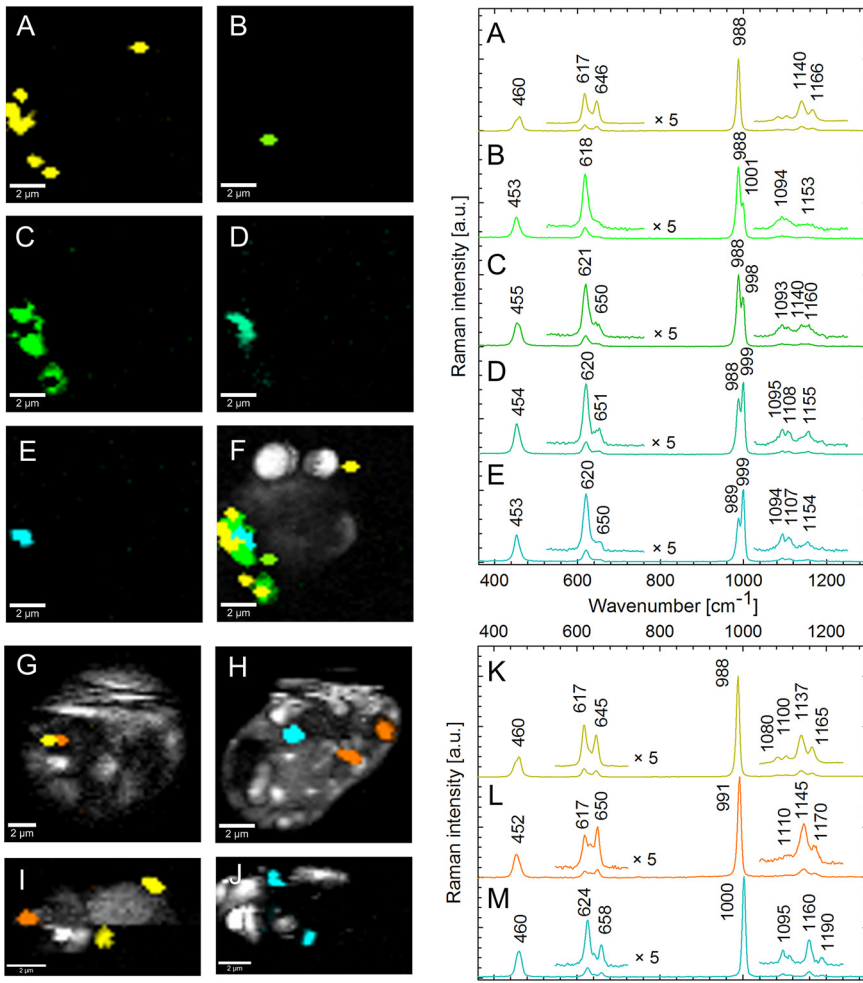


**FIG 5** Raman maps and spectra of barite and celestite crystals in diplomemids cultivated with equimolar amounts of  $\text{Sr}^{2+}$  and  $\text{Ba}^{2+}$  in the medium. (A to F) A single cell of *N. karyoxenos* containing cocrystallized fractions dominated by celestite in the central part (E; cyan) with gradually overlapping barite (B to D; shades of green) toward the periphery of its pure fraction (A; yellow), and the merged Raman map of of panels A to E (F). The limited spatial resolution of Raman microscopy did not allow distinguishing conglomerates of pure-species microcrystals from a single crystal with a variable elemental composition. (G to M) Two cells of *Lacrimia* sp. YPF1808 (G and H) and two cells *L. lanifica* (I and J) contained pure barite (K; yellow) and celestite (M; blue) and homogeneously mixed crystals of  $(\text{Ba,Sr})\text{SO}_4$  (L; orange).

fecal pellets contained undigested chlorophyll, carotenoids with remnants of lipids, calcite particles, and contaminating polystyrene microplastic particles, but lacked celestite crystals (Fig. 6B).

## DISCUSSION

The most studied biominerals in protists are extracellular calcite scales of haptophytes and silicate frustules of diatoms, while studies on intracellular mineral crystals are far less common (38). After more than a century since the skeletons of marine acanthareans and freshwater streptophytes were found to contain celestite (16) and barite (39), respectively, we have identified potent accumulators of  $\text{Ba}^{2+}$  and  $\text{Sr}^{2+}$  in an unexpected group of eukaryotes, the diplomemids.

The heterotrophic diplomemids are widespread in the oceans and, as recently described, in astonishing abundance and diversity (31, 33). Despite their abundance and extreme diversity, diplomemid flagellates remain a poorly known group of protists (34) that are abundant from the surface to the deep sea, with a wide peak in the

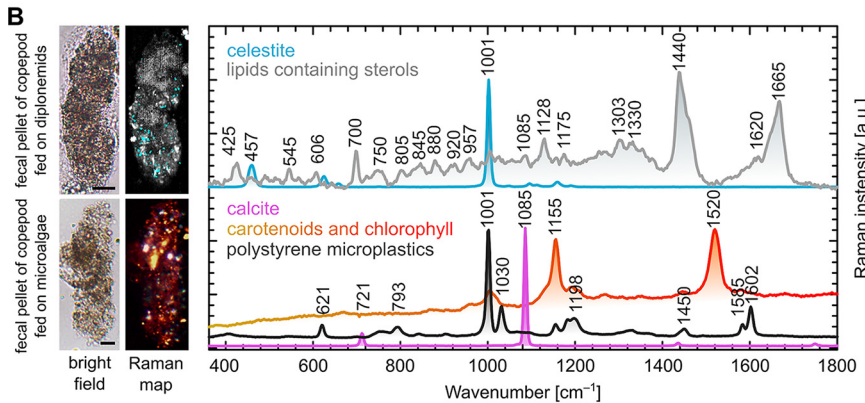
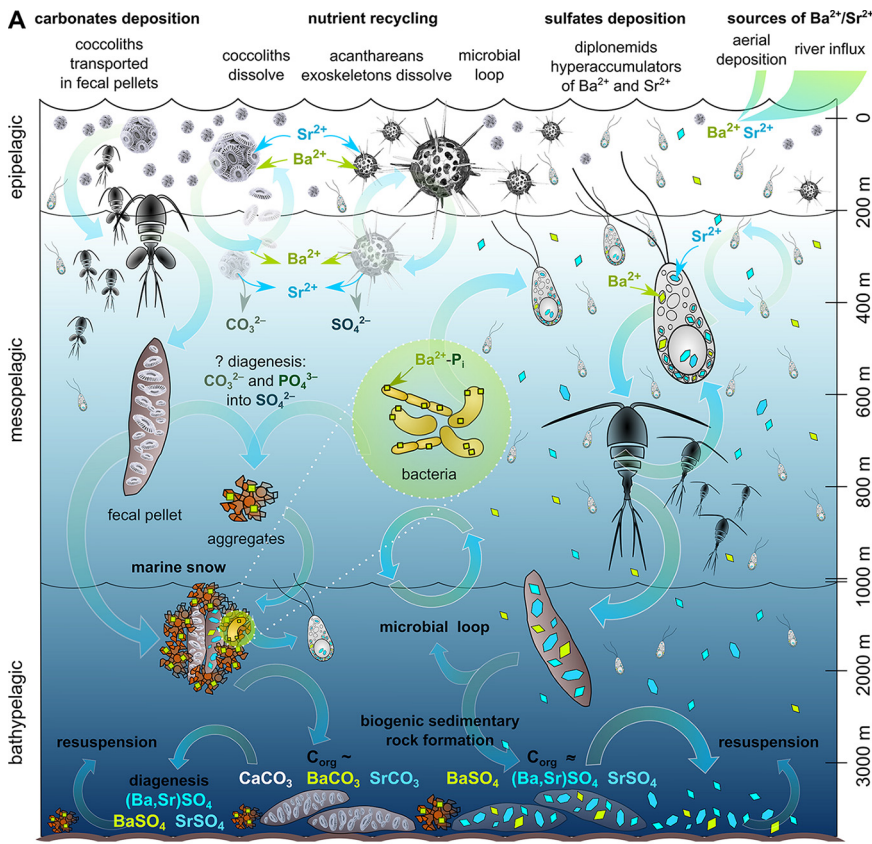


**FIG 6** Schematic representation of the biological impact on Ba<sup>2+</sup> and Sr<sup>2+</sup> cycling in the oceans. (A) Hypothetical scenario of trace elements inlet, plankton uptake, recycling, and sedimentary deposition. The major source of trace elements is driven by river influx and less prominently by aerial deposition (9) and is mostly balanced by the same amount of total deposition in sediments, correlated with the total marine productivity and particulate organic matter deposition (24). A great proportion of these trace elements is being recycled by living organisms after release from dead cells. Acantharea (image adapted from referene 69) take up a substantial portion of Sr<sup>2+</sup> and Ba<sup>2+</sup>, which are further recycled in upper 400 m (25). Coccolithophorids build their scales from calcium carbonate with minor amounts of Ba<sup>2+</sup> and Sr<sup>2+</sup> that are proportional to the seawater contents (22), being partially recycled upon dissolution or transported to the marine sediments in fecal pellets (24). The Ba<sup>2+</sup> accumulated by bacteria sediments in the aggregates of marine snow (26) or is recycled. We highlighted diplonemids as potential players in the marine cycle of both elements and drivers of biogenic formation of celestite and barite crystals found in suspended matter everywhere in the world oceans (24), and they can also feed on bacteria or particulate organic matter or scavenge the dead bodies of zooplankton as major heterotrophic protists in the mesopelagic zone. (B) Raman microscopy analysis of fecal pellets produced by copepods experimentally fed with diplonemids, which contained celestite crystals (cyan) and undigested lipids, including sterols (gray). In the control samples of copepods fed with microalgae, fecal pellets contained undigested carotenoids, chlorophyll (yellow-orange-red), and calcite particles (pink), with unexpected particles of polystyrene microplastics (measured as a single spectrum [not shown on the Raman map]). Scale bars, 20 μm.

mesopelagic zone (32, 33, 40, 41). The high capacity of intracellular  $\text{Sr}^{2+}$  and  $\text{Ba}^{2+}$  accumulation in some diplonemids outperforms that of any other reported organisms (10, 13, 21, 42–44). Indeed, while the intracellular concentration of  $\text{Sr}^{2+}$  in the most efficient accumulators known thus far (yeasts, desmids, and cyanobacteria) reaches a maximum of  $220 \text{ mg}\cdot\text{g}^{-1}$  per dry weight (1, 10, 43), *N. karyoxenos* contains as much as  $340 \text{ mg}\cdot\text{g}^{-1}$   $\text{Sr}^{2+}$  together with  $120 \text{ mg}\cdot\text{g}^{-1}$   $\text{Ba}^{2+}$ , which in the form of sulfate represents 90% of the cellular dry mass, pointing to the unique  $\text{Sr}^{2+}$  and  $\text{Ba}^{2+}$  accumulation capacity of this diplonemid, while both *Lacrimia* species are slightly less potent in this respect (Table 1).

Interestingly, when both trace elements are provided in equimolar concentrations, diplonemids form pure celestite and barite and/or mixed forms of  $(\text{Ba},\text{Sr})\text{SO}_4$ , apparently not discriminating one element over the other. Hence, we explain the higher content of  $\text{Sr}^{2+}$  over  $\text{Ba}^{2+}$  inside the crystals by the higher availability of the former element in seawater. Although the mechanisms behind intracellular accumulation of  $\text{Sr}^{2+}$  and  $\text{Ba}^{2+}$  are largely unknown, it has been suggested that mineral crystals typically occur in membrane-bounded compartments or vacuoles, in which they are formed from supersaturated solutions via precisely regulated nucleation (13). The  $\text{Sr}^{2+}$  uptake and transportation within eukaryotic cells have been shown to occur via commonly present transporters of divalent cations, i.e., the  $\text{Ca}^{2+}$  uniporter and  $\text{H}^+/\text{Ca}^{2+}$  antiporter (45, 46). The diplonemid nuclear genome is not yet available, but these transporters have been documented in the related kinetoplastid *Trypanosoma brucei* (47). Although the reported affinity to  $\text{Ca}^{2+}$  and  $\text{Sr}^{2+}$  is usually comparable (45, 46), some organisms including diplonemids clearly favor  $\text{Ba}^{2+}$  and  $\text{Sr}^{2+}$  over  $\text{Ca}^{2+}$  (10). When such vacuoles contain sulfate solutions, they may function as a “sulfate trap” for those cations that precipitate easily in the presence of sulfates (2). At the same time, we did not observe  $\text{CaSO}_4$  or any of its forms (gypsum, bassanite, anhydrite, etc.), even though the concentration of  $\text{Ca}^{2+}$  in the cultivation medium or in the environment is several orders of magnitude higher than that of  $\text{Sr}^{2+}$  and  $\text{Ba}^{2+}$ .

Densities of celestite and barite of  $3.9 \text{ g}\cdot\text{cm}^{-3}$  and  $4.5 \text{ g}\cdot\text{cm}^{-3}$ , respectively, have been repeatedly reported as statoliths in ciliates or charophytic algae (13, 17, 18). In comparison to the seawater density of  $1.03 \text{ g}\cdot\text{cm}^{-3}$  and typical cell density range between  $0.985$  and  $1.156 \text{ g}\cdot\text{cm}^{-3}$ , the heavy crystals may help maintain appropriate buoyancy by counterbalancing light lipid droplets ( $0.86 \text{ g}\cdot\text{cm}^{-3}$ ) (37, 48). Indeed, the impact of celestite crystals is substantial, since they may increase the overall density of *Lacrimia* sp. YPF1808 and *N. karyoxenos* by up to 9% and 27%, respectively (Table S2). According to Stokes' law for small particles of low Reynolds numbers, the barite/celestite ballasting can significantly increase the sedimentary velocity for up to 50 to 200 m per month or 0.5 to 2 km per year (Table S2). Hence, while the function of biomineralization in diplonemids remains unknown, we speculate that they may benefit from gravitropic sensing, which would allow directed movement and/or enable passive sedimentation. Another intriguing impact of barite and celestite is associated with their propensity to strong absorption of UV and blue light (49). Hence, in surface waters, these minerals may contribute to UV protection. It is reasonable to assume that by forming celestite, protists adjust their inner osmolarity, the principle analogical to the formation of other cell inclusions, such as oxalate, calcite, or polyphosphate, that are either dissolved and osmotically active or crystallized or polymerized and osmotically inactive inside a vacuole (13, 50).

Celestite-forming acanthareans are considered key players in the upper 400 m of the ocean, yet do not contribute to the sedimentary rock formation, as their skeletons dissolve upon decay of their cells (25). Coccolithophorids and bacteria produce carbonates (44) and/or phosphates (26) of  $\text{Ba}^{2+}/\text{Sr}^{2+}$ , which can also be converted to sulfates either on the bacterial extracellular polymeric substances or in the microenvironment of decaying matter of marine snow aggregates in the process of diagenesis (26). In the chemical continuum between pure barite and celestite, the latter represents 10 to 30%

(24), gradually decreasing, depending on the depth (11, 12). The majority of biogenic particulate barite and celestite is recycled by simple dissolution (25), microbial loop (26), or resuspension of sediments (24). However, the overall influx into the system is balanced by sedimentary deposition (9, 24), which might have a biological driver. Seminal work of Dehairs et al. (24) scrutinized all potential sources of particulate barite and celestite, and they did not find experimental support for either  $\text{Ba}^{2+}$  incorporation in siliceous plankton or precipitations on decaying organic matter in sulfate-enriched microenvironments. Hence, they ultimately favored the biogenic origin of particulate barite/celestite being hypothetically formed by microorganisms inhabiting the high-productivity mesopelagic zone (24) only to remain unknown since then. These predictions nicely correlate with our measurements in diplonemids, indicating that micron-sized celestite and sometimes barite crystals of variable Ba-Sr ratios (Fig. 2 to 5) are scattered throughout the water column of the world's oceans, with the highest prevalence in the mesopelagic zone (32). Moreover, particulate barite/celestite is often found in fecal pellets and aggregates of marine snow, and finally, in the sediments (24, 27, 32). By providing celestite-containing diplonemids to filter-feeding copepods, we found undigested celestite in their fecal pellets (Fig. 6), the main transport system of micrometric biominerals into the sediments, although the majority is recycled (24). Thus, diplonemids may be involved in  $\text{Ba}^{2+}/\text{Sr}^{2+}$  cycling and/or in sedimentary deposition of celestite or barite. Since these protists likely emerged during the Neoproterozoic era (590 to 900 million years ago [MYA]), overlapping with the Ediacaran period (51), their impact on biogenic marine sediments may cover several geological eras. The coccolithophores appeared around the same time as diplonemids, yet the onset of carbonate biomineralization has been timed to  $\sim 200$  MYA (52).

As another ecological addition to the big picture of  $\text{Ba}^{2+}/\text{Sr}^{2+}$  cycling, diplonemids have been shown to ingest bacteria as one of their sources of nutrition (30); if bacteria were loaded with  $\text{Ba}^{2+}/\text{Sr}^{2+}$  in the form of (poly)phosphates, as reported elsewhere (26), diplonemids may further transform it into barite upon digestion. Additionally, diplonemids are likely to feed on the organic matter of marine snow providing pre-concentrated  $\text{Ba}^{2+}$ , in which case they may accumulate more  $\text{Ba}^{2+}$  than  $\text{Sr}^{2+}$ . In principle, we experimentally supported such a scenario upon doping the cells with equimolar  $\text{Ba}^{2+}$  and  $\text{Sr}^{2+}$  concentrations (Fig. 5). Finally, we do not exclude that some species of diplonemids to be described in future would prefer  $\text{Ba}^{2+}$  over  $\text{Sr}^{2+}$  or that there are other as-yet-unknown microbial bioaccumulators of these trace elements.

Based on the ability of some diplonemids to store massive amounts of celestite and to lesser extent barite, we speculate that more as-yet-unknown diplonemid species may qualify as impactful players of  $\text{Ba}^{2+}/\text{Sr}^{2+}$  flow through the food web, eventually influencing the sedimentary records.

## MATERIALS AND METHODS

**Cell cultures, cultivation, and light microscopy.** For all experiments, axenic cultures were grown in seawater-based Hemi medium (see Table S1 in the supplemental material) supplemented with 1% horse serum and 0.025 g/liter LB broth powder (53). An artificial seawater medium lacking  $\text{Sr}^{2+}$ ,  $\text{Ba}^{2+}$ , and sulfates was prepared from 288 mM NaCl, 8 mM KCl, 718 mM KBr, 100 mM  $\text{MgCl}_2$ , 12 mM  $\text{CaCl}_2$ , 40 mM  $\text{HBO}_3$ , and 60 mM NaF, supplemented with 1% (vol/vol) heat-inactivated horse serum (Sigma-Aldrich) and 25 mg LB broth powder (Amresco). The medium was used as rinsing solution for preparation of ICP-MS samples and cell microcrystal depletion to be measured via quantitative phase imaging (QPI) (see below). For  $\text{Ba}^{2+}$  loading experiments,  $\text{BaCl}_2$  was added in equimolar amounts with respect to naturally occurring (88  $\mu\text{M}$ )  $\text{Sr}^{2+}$  (12).

Axenic clonal cultures of 17 species of diplonemids were grown either at 27°C (*Paradiplonema papillatum* ATCC 50162), 22°C (*Namystinia karyoxenos* YPF1621), or 13°C (of *D. aggregatum* YPF1605, *D. japonicum* YPF1604, *Flectonema* sp. DT1601, *Hemistasia phaeocysticola*, *Lacrimia lanifica* JW1601, *Lacrimia* sp. YPF1808, *Rhynchopus* sp. YZ270 cl. 10.3, *Rhynchopus* sp. YZ270 cl. 9, *Rhynchopus* sp. DT0301, *Rhynchopus humris* YPF1505, *R. euleioides* ATCC 50226, *R. serpens* YPF1515, and *Sulcionema specki* YPF1618). *P. papillatum* and *R. euleioides* were isolated from coastal surface waters (United States) in 1985 and 1986, respectively. The remaining species originated either from coastal seawater around Japan or from Enoshima Aquarium (Kanagawa, Japan) and were continuously maintained in culture for 1 to 7 years prior to the analyses. The identity of not-yet-formally described species was established based on the 18S rRNA sequences as described previously (54). Dense cultures of trophic cells (55) were harvested by centrifugation at  $3,000 \times g$  for all subsequent analyses.

Light microscopy images and videos were taken with an Olympus BX53 microscope equipped with a DP72 microscope digital camera using CellSens software v. 1.11 (Olympus) and processed with GIMP v. 2.10.14, Lrfan View v. 4.54, and Image J v. 1.51 software. Polarized microscopy was performed using crossed polarizers installed to a Raman microscope (as specified below).

**Environmental sampling.** Zooplankton was collected in the Bay of Villefranche sur Mer, France (43°40'N, 7°19'E) with a 10-min haul from 10 m to the surface, using a 20- $\mu$ m-mesh-size plankton net. Captured copepods were transferred into 0.5 liters of freshly filtered natural seawater and starved for 12 h. *Centropages typicus*, *Temora longicornis*, and *Acartia* sp. were then picked under a dissection microscope. All experiments were carried out at cultivation temperature of the prey species of diplonemids (13°C for *Lacrimia* sp. YPF1808, room temperature for *N. karyoxenos*). Ten copepods were kept in 20 mL of diplonemid culture ( $10^5$  cells mL<sup>-1</sup>) for 5 days, after which their fecal pellets were collected under a dissection microscope and immediately analyzed by Raman microscopy (as specified below).

**Raman microscopy.** For the *in situ* determination of the chemical composition of intracellular structures, a confocal Raman microscope (alpha300 RSA; WITec, Germany) was used as previously described (56–60). To immobilize the fast-moving flagellates on the quartz slide, 5  $\mu$ L of the cell pellet was mixed with 5  $\mu$ L of 1% (wt/vol) solution of low-melting-point agarose (catalog number 6351.5; Carl Roth, Germany), immediately spread as a single-cell layer between a quartz slide and coverslip, and sealed with CoverGrip sealant (Biotium, USA). Two-dimensional Raman maps were obtained with laser excitation at 532 nm (20 mW power at the focal plane) and oil-immersion objective UPlanFLN 100 $\times$ , numerical aperture (NA) 1.30, or water-immersion objective UPlanSApo 60 $\times$ , NA 1.20 (Olympus, Japan). A scanning step size of 200 nm in both directions and an integration time of 100 ms per voxel were used. A minimum of 30 cells were measured for each strain. Raman chemical maps were constructed by multivariate decomposition of the baseline-corrected spectra into the spectra of pure chemical components by using Project Plus 5.1 software (WITec, Germany).

**TEM, TEM-ED, and TEM-EDX.** The protocol for the basic sample preparation of all kinds of electron microscopy approaches listed here is described in detail elsewhere (61). We used it with minor modifications, as stated below. Cell pellets were transferred to specimen carriers and immediately frozen in the presence of 20% (wt/vol) bovine serum albumin solution using a high-pressure freezer (Leica EM ICE, Leica Microsystems, Austria). Freeze substitution was performed in the presence of 2% osmium tetroxide diluted in 100% acetone at  $-90^\circ\text{C}$ . After 96 h, specimens were warmed to  $-20^\circ\text{C}$  at a step of  $5^\circ\text{C}/\text{h}$ . After another 24 h, the temperature was increased to  $3^\circ\text{C}$  ( $3^\circ\text{C}/\text{h}$ ). At room temperature, samples were washed in acetone and infiltrated with 25%, 50%, and 75% acetone/resin mixture for 1 h at each step. Finally, samples were infiltrated in 100% resin and polymerized at  $60^\circ\text{C}$  for 48 h. Semithin (250 nm) and ultrathin (70 nm) sections were cut using a diamond knife, placed on copper grids, and stained with uranyl acetate and lead citrate. TEM micrographs were taken with a Mega View III camera (SIS) using a JEOL 1010 TEM operating at an accelerating voltage of 80 kV.

For TEM-EDX, 10  $\mu$ L of pelleted *L. lanifica* cells was spread over a holey carbon-coated copper grid, washed twice with 10  $\mu$ L of distilled water in order to reduce the sea salts from the culture medium, and allowed to dry by evaporation at ambient temperature. Semithin sections of resin-infiltrated blocks of *N. karyoxenos* were prepared as stated above. For the identification of the crystalline phase, sections were studied by TEM on an FEI Tecnai 20 system (LaB6, 120 kV) equipped with an Olympus SIS charge-coupled-device camera Veleta (2,048 pixels) and an EDAX windowless EDX detector Apollo XLTW for elemental analysis. The diffraction data were collected by means of 3D electron diffraction (ED) (62). The data processing was carried out using PETS software (63). Structure solution and refinement were performed in the computing system Jana2006 (64).

**Cryo-scanning electron microscopy with EDX.** Cells pellets were high-pressure frozen as described above and transferred into a Leica ACE 600 preparation chamber (Leica Microsystems, Austria) precooled at  $-135^\circ\text{C}$ , fractured with a scalpel, freeze-etched at  $-100^\circ\text{C}$  for 1 min, and sputter-coated with 2.5 nm of gold-palladium at  $-125^\circ\text{C}$ . Specimens were transferred under vacuum using transfer system VCT100 (Leica Microsystems, Austria) and observed with a Magellan 400L SEM (FEI, Czech Republic and USA) precooled at  $-125^\circ\text{C}$  (cryo-SEM). Topographical images and EDX measurements were obtained using an EDT detector and EDAX detector (Octane Elect Super; EDAX, USA), respectively, either at 5 keV/0.1 NA or 10 keV/0.8 NA. The taken spectra were analyzed with EDAX TEAM software and quantified by the eZAF method.

**Serial block-face SEM.** The sample preparation of *Lacrimia* sp. YPF1808 by the high-pressure freezing technique followed the protocol for TEM sample preparation. After freeze-substitution, the samples were subsequently stained with 1% thiocarbonylhydrazide in 100% acetone for 1.5 h, 2% OsO<sub>4</sub> in 100% acetone for 2 h at room temperature, and 1% uranyl acetate in 100% acetone overnight at  $4^\circ\text{C}$ . After every staining step, the samples were washed 3 times with 100% acetone for 15 min. Samples were then infiltrated with 25%, 50%, or 75% acetone-resin mixture for 2 h at each step, and finally infiltrated in 100% Hard Resin Plus 812 (EMS) overnight and polymerized at  $62^\circ\text{C}$  for 48 h. Resin-embedded blocks were trimmed and imaged using an Apreo SEM equipped with a VolumeScope (Thermo Fisher Scientific, Germany). Serial images were acquired at 3.5 keV, 50 pA, 40 Pa with a resolution of 6 nm, 100-nm slice thickness, and dwell time per pixel of 4  $\mu$ s. Image data were processed in Microscopy Image Browser v2.702 (65) and Amira v2020.2. The resin-embedded blocks were also collected in the form of 1- $\mu$ m-thick sections on a silicon wafer and analyzed by SEM-EDX (Magellan 400L system, as described above).

Based on volumetric data, we calculated the percentage of increase in cell density based on measured volumes of crystals compared to the theoretical crystal-free cells of the same volume and reported average theoretical density of 1.07 g·cm<sup>-3</sup> (37).

**ICP-MS.** For analysis of Ba and  $^{88}\text{Sr}$  concentrations, cultures were grown in triplicates, counted, and washed three times with 1 M sorbitol solution (for *P. papillatum*, *D. japonicum*, and *Rhynchopus* YZ270 cl. 10) or Sr- and Ba-free artificial seawater rinsing solution (see above) (for *L. lanifica* JW1601, *Lacrimia* sp. 1808, and *N. karyoxenos*) to remove  $\text{Ba}^{2+}$  and  $\text{Sr}^{2+}$  present in the cultivation medium. Cultivated cells were harvested by centrifugation and rinsed twice with 50 mL and once with 2 mL of the rinsing solution, and the resulting pellets were freeze-dried. A 0.5-mL digestion acid mix (425  $\mu\text{L}$  of 70%  $\text{HClO}_4$  and 75  $\mu\text{L}$  of 69%  $\text{HNO}_3$ ) prepared as described elsewhere (66) was added directly to the dried biomass. The digestion was done using a Fuji PXG4 Thermoblock (AHF Analysentechnik AG, Germany). After evaporation of the acid mix, 0.5 mL of 5% HCl was added to each test tube to redissolve the salts. The glass tubes were heated to 90°C for 1 h to obtain clear solutions. The final volume of 1.5 mL was adjusted with double-distilled  $\text{H}_2\text{O}$ . Appropriate dilutions were made with 0.2%  $\text{HNO}_3$ . Indium was added as an internal standard at 1 ng/mL to each test solution. The ICP multielement standard solution VI (Merck, Germany) was used to prepare standard curves. Analyses were done using an inductively coupled plasma sector-field mass spectrometer (ICP sfMS) Element XR-2 with jet interface (Thermo Fisher Scientific, Germany) following a described protocol (67). Medium resolution of 4,000 was used in Ba and  $^{88}\text{Sr}$  measurements in triplicate of each technical replicate, with the highest precision and lowest relative standard deviation. Additionally, the elemental composition of samples of standard growth medium and artificial seawater medium without sulfates,  $\text{Ba}^{2+}$ , or  $\text{Sr}^{2+}$  were analyzed.

**Holographic microscopy and QPI.** Samples for holographic microscopy were immobilized prior to measurement as described above for Raman microscopy. Imaging was performed at the Q-Phase microscope (Tescan Orsay Holding, Czech Republic). The holographic Q-Phase microscope is equipped with halogen lamp illumination through an interference filter ( $\lambda_{1/4}$ ) 650 nm, 10 nm full-width, half-maximal) and microscope objective (Nikon Plan Fluor oil immersion, 60 $\times$ , numerical aperture 1.4, providing lateral resolution of 0.57  $\mu\text{m}$ ). The numerical reconstruction of acquired data was performed using Q-Phase software (Tescan Orsay Holding, Czech Republic). The technique enables automated cell segmentation and quantitative analysis of cellular mass based on the specific proportions of thickness and refractive indices of measured cells in comparison to the reference (68). Due to the high variability of cell contents and sizes, at least 150 cells were analyzed for each strain. Because crystalline inclusions caused artifacts during capturing due to the big difference in refractive indices, we analyzed crystal-free cells cultivated in the artificial seawater medium lacking  $\text{Sr}^{2+}$ ,  $\text{Ba}^{2+}$ , and sulfates (as specified above). We calculated the total dry mass of the cells as the sum of crystal-free cells, measured by holographic microscopy, and  $\text{SrSO}_4$  and  $\text{BaSO}_4$  amounts measured via ICP-MS. The dry weight ratios of trace elements measured via ICP-MS were calculated based on the total dry weight of corresponding strains.

**Statistical data analysis.** Statistical analysis was conducted using SigmaPlot v. 12.5 and SPSS v. 23.0. Logarithmically normalized data were subjected to statistical tests (one-way analysis of variance [ANOVA] and Tukey's *post hoc*) on an alpha level of 0.05. Calculations of standard errors of the means based on independent methods (i.e., ICP-MS quantification and QPI dry mass quantification) with different levels of variability were done according to mathematical conversion using Taylor expansion.

**Data availability.** All data generated or analyzed during this study are included in the published article and its supplemental material files.

## SUPPLEMENTAL MATERIAL

Supplemental material is available online only.

**MOVIE S1**, MOV file, 12.6 MB.

**MOVIE S2**, MOV file, 12.9 MB.

**FIG S1**, PDF file, 0.2 MB.

**FIG S2**, PDF file, 0.1 MB.

**FIG S3**, PDF file, 0.1 MB.

**FIG S4**, PDF file, 0.1 MB.

**FIG S5**, PDF file, 0.1 MB.

**TABLE S1**, PDF file, 0.04 MB.

**TABLE S2**, PDF file, 1.8 MB.

## ACKNOWLEDGMENTS

This work was supported by ERD Funds projects OPVVV 16\_019/0000759 (to J.L.), 15\_003/0000336 KOROLID (to H.K. and B.S.N.H.), and 16\_013/0001775 (to D.T., J.T., and M.V.); ERC CZ LL1601 (to J.L.); Czech Bioimaging grant LM2018129 (to J.P., D.T., J.T., and M.V.); Czech Science Foundation grant 21-261155 (to J.P. and P.M.); Czech Academy of Sciences travel grant VAJVA-19-68 (to D.T.); and the Gordon and Betty Moore Foundation GBMF9354 (to J.L.). We acknowledge CzechNanoLab Research Infrastructure and the grant support LM2018110 (to M.K.) and the Light Microscopy Core Facility and the grant support 18\_046/0016045 (to J.P.) for help with holographic microscopy.

D.T., J.P., and J.L. designed the research; D.T., J.P., J.T., M.V., S.N.H.B., R.S., and M.K. performed the research; J.P., D.T., J.T., M.V., H.K., P.M., and J.L. analyzed the data; J.T.,

M.V., H.K., P.M., R.S., and M.K. contributed reagents and analytic tools; J.P., D.T., and J.L. wrote the paper.

We declare no conflict of interest.

## REFERENCES

- Avery SV, Smith SL, Ghazi AM, Hoptroff MJ. 1999. Stimulation of strontium accumulation in linoleate-enriched *Saccharomyces cerevisiae* is a result of reduced  $\text{Sr}^{2+}$  efflux. *Appl Environ Microbiol* 65:1191–1197. <https://doi.org/10.1128/AEM.65.3.1191-1197.1999>.
- Krejci MR, Wasserman B, Finney L, McNulty I, Legnini D, Vogt S, Joester D. 2011. Selectivity in biomineralization of barium and strontium. *J Struct Biol* 176:192–202. <https://doi.org/10.1016/j.jsb.2011.08.006>.
- Bowen HJM, Dymond JA. 1955. Strontium and barium in plants and soils. *Proc R Soc Lond B Biol Sci* 144:355–368.
- Pors Nielsen S. 2004. The biological role of strontium. *Bone* 35:583–588. <https://doi.org/10.1016/j.bone.2004.04.026>.
- Bhoelan BS, Stevering CH, van der Boog ATJ, van der Heyden MAG. 2014. Barium toxicity and the role of the potassium inward rectifier current. *Clin Toxicol* 52:584–593. <https://doi.org/10.3109/15563650.2014.923903>.
- Fukuda SY, Iwamoto K, Atsumi M, Yokoyama A, Nakayama T, Ishida K-I, Inouye I, Shiraiwa Y. 2014. Global searches for microalgae and aquatic plants that can eliminate radioactive cesium, iodine and strontium from the radio-polluted aquatic environment: a bioremediation strategy. *J Plant Res* 127:79–89. <https://doi.org/10.1007/s10265-013-0596-9>.
- Walker JB. 1953. Inorganic micronutrient requirements of *Chlorella*. I. Requirements for calcium (or strontium), copper, and molybdenum. *Arch Biochem Biophys* 46:1–11. [https://doi.org/10.1016/0003-9861\(53\)90163-5](https://doi.org/10.1016/0003-9861(53)90163-5).
- Bolland MJ, Grey A. 2016. Ten years too long: strontium ranelate, cardiac events, and the European Medicines Agency. *Br Med J* 354:i5109. <https://doi.org/10.1136/bmj.i5109>.
- Moore JW. 1991. Inorganic contaminants of surface water: research and monitoring priorities, 1st ed. Springer US, New York, NY.
- Cam N, Benzerara K, Georgelin T, Jaber M, Lambert JF, Poinot M, Skouri-Panet F, Cordier L. 2016. Selective uptake of alkaline earth metals by cyanobacteria forming intracellular carbonates. *Environ Sci Technol* 50:11654–11662. <https://doi.org/10.1021/acs.est.6b02872>.
- Paytan A, Griffith EM. 2007. Marine barite: recorder of variations in ocean export productivity. *Deep Sea Res II* 54:687–705. <https://doi.org/10.1016/j.dsr2.2007.01.007>.
- Griffith EM, Paytan A. 2012. Barite in the ocean: occurrence, geochemistry and palaeoceanographic applications. *Sedimentology* 59:1817–1835. <https://doi.org/10.1111/j.1365-3091.2012.01327.x>.
- Raven JA, Knoll AH. 2010. Non-skeletal biomineralization by eukaryotes: matters of moment and gravity. *Geomicrobiol J* 27:572–584. <https://doi.org/10.1080/01490451003702990>.
- Langer G, Nehrke G, Thoms S, Stoll H. 2009. Barium partitioning in coccoliths of *Emiliania huxleyi*. *Geochim Cosmochim Acta* 73:2899–2906. <https://doi.org/10.1016/j.gca.2009.02.025>.
- Monnin C, Cividini D. 2006. The saturation state of the world's ocean with respect to (Ba,Sr)SO<sub>4</sub> solid solutions. *Geochim Cosmochim Acta* 70:3290–3298. <https://doi.org/10.1016/j.gca.2006.04.002>.
- Bütschli O. 1906. Über die chemische Natur der Skeletsubstanz der Acantharia. *Zool Anz* 30:784–789.
- Hemmersbach R, Krause M, Bräucker R, Ivanova K. 2005. Graviperception in ciliates: steps in the transduction chain. *Adv Space Res* 35:296–299. <https://doi.org/10.1016/j.asr.2005.03.024>.
- Brook AJ, Fotheringham A, Bradly J, Jenkins A. 1980. Barium accumulation by desmids of the genus *Closterium* (Zygnemaphyceae). *Br Phycol J* 15: 261–264. <https://doi.org/10.1080/00071618000650251>.
- Goody AJ, Nott JA. 1982. Intracellular barite crystals in two Xenophyphores, *Aschemonella ramuliformis* and *Galatheaemmina* sp. (Protozoa: Rhizopoda) with comments on the taxonomy of *A. ramuliformis*. *J Mar Biol Ass* 62:595–605. <https://doi.org/10.1017/S0025315400019779>.
- Fresnel J, Galle P, Gayral P. 1979. Résultats de la microanalyse des cristaux vacuolaires chez deux Chromophytes unicellulaires marines: *Exanthemachrysis gayraliae*, *Pavlova* sp. (Prymnesiophyceae, Pavlovaceae). *C R Hebd Seances Ser D Sci Nat* 288:823–825.
- Martignier A, Filella M, Pollok K, Melkonian M, Bensimon M, Barja F, Langenhorst F, Jaquet JM, Ariztegui D. 2018. Marine and freshwater micropearls: biomineralization producing strontium-rich amorphous calcium carbonate inclusions is widespread in the genus *Tetraselmis* (Chlorophyta). *Biogeosciences* 15:6591–6605. <https://doi.org/10.5194/bg-15-6591-2018>.
- Stoll HM, Rosenthal Y, Falkowski P. 2002. Climate proxies from Sr/Ca of coccolith calcite: Calibrations from continuous culture of *Emiliania huxleyi*. *Geochim Cosmochim Acta* 66:927–936. [https://doi.org/10.1016/S0016-7037\(01\)00836-5](https://doi.org/10.1016/S0016-7037(01)00836-5).
- Dymond J, Collier R. 1996. Particulate barium fluxes and their relationships to biological productivity. *Deep Res Part II Top Stud Oceanogr* 43: 1283–1308. [https://doi.org/10.1016/0967-0645\(96\)00011-2](https://doi.org/10.1016/0967-0645(96)00011-2).
- Dehairs F, Chesselet R, Jedwab J. 1980. Discrete suspended particles of barite and the barium cycle in the open ocean. *Earth Planet Sci Lett* 49: 528–550. [https://doi.org/10.1016/0012-821X\(80\)90094-1](https://doi.org/10.1016/0012-821X(80)90094-1).
- De Deckker P. 2004. On the celestite-secreting Acantharia and their effect on seawater strontium to calcium ratios. *Hydrobiologia* 517:1–13. <https://doi.org/10.1023/B:HYDR.0000027333.02017.50>.
- Martinez-Ruiz F, Jroundi F, Paytan A, Guerra-Tschuschke I, Abad MDM, González-Muñoz MT. 2018. Barium bioaccumulation by bacterial biofilms and implications for Ba cycling and use of Ba proxies. *Nat Commun* 9: 1619. <https://doi.org/10.1038/s41467-018-04069-z>.
- Bishop JKB. 1988. The barite-opal-organic carbon association in oceanic particulate matter. *Nature* 332:341–343. <https://doi.org/10.1038/332341a0>.
- Horner TJ, Pryer HV, Nielsen SG, Crockford PW, Gauglitz JM, Wing BA, Ricketts RD. 2017. Pelagic barite precipitation at micromolar ambient sulfate. *Nat Commun* 8:1342. <https://doi.org/10.1038/s41467-017-01229-5>.
- Kostygov AY, Karnkowska A, Votýpka J, Tashyreva D, Maciszewski K, Yurchenko V, Lukeš J. 2021. Euglenozoa: taxonomy, diversity and ecology, symbioses and viruses. *Open Biol* 11:200407. <https://doi.org/10.1098/rsob.200407>.
- Prokopchuk G, Korytář T, Juricová V, Majstorović J, Horák A, Šimek K, Lukeš J. 2022. Trophic flexibility of marine diplonemids: switching from osmotrophy to bacterivory. *ISME J* 16:1409–1419. <https://doi.org/10.1038/s41396-022-01192-0>.
- Tashyreva D, Simpson AGB, Prokopchuk G, Škodová-Sveráková I, Butenko A, Hammond M, George EE, Flegontova O, Záhonová K, Faktorová D, Yabuki A, Horák A, Keeling PJ, Lukeš J. 2022. Diplonemids: a review on “new” flagellates on the oceanic block. *Protist* 173:125868. <https://doi.org/10.1016/j.protis.2022.125868>.
- Flegontova O, Flegontov P, Malviya S, Audic S, Wincker P, de Vargas C, Bowler C, Lukeš J, Horák A. 2016. Extreme diversity of diplonemid eukaryotes in the Ocean. *Curr Biol* 26:3060–3065. <https://doi.org/10.1016/j.cub.2016.09.031>.
- Flegontova O, Flegontov P, Londoño Castañeda AP, Walczowski W, Šantić D, Edgcomb VP, Lukeš J, Horák A. 2020. Environmental determinants of the distribution of planktonic diplonemids and kinetoplastids in the oceans. *Environ Microbiol* 22:4014–4031. <https://doi.org/10.1111/1462-2920.15190>.
- de Vargas C, Audic S, Henry N, Decelle J, Mahé F, Logares R, Lara E, Berney C, Le Bescot N, Probert I, Carmichael M, Poulain J, Romac S, Colin S, Aury J-M, Bittner L, Chaffron S, Dunthorn M, Engelen S, Flegontova O, Guidi L, Horák A, Jaillon O, Lima-Mendez G, Lukeš J, Malviya S, Morard R, Mulot M, Scalco E, Siano R, Vincent F, Zingone A, Dimier C, Picheral M, Searson S, Kandels-Lewis S, Tara Oceans Coordinators, Acinas SG, Bork P, Bowler C, Gorsky G, Grimsley N, Hingamp P, Iudicone D, Not F, Ogata H, Pesant S, Raes J, Sieracki ME, Speich S, et al. 2015. Eukaryotic plankton diversity in the sunlit ocean. *Science* 348:1261605. <https://doi.org/10.1126/science.1261605>.
- Mukherjee I, Salcher MM, Andrei AŞ, Kavagutti VS, Shabarova T, Grujić V, Haber M, Layoun P, Hodoki Y, Nakano SI, Šimek K, Ghai R. 2020. A freshwater radiation of diplonemids. *Environ Microbiol* 22:4658–4668. <https://doi.org/10.1111/1462-2920.15209>.
- Zhou L, Mernagh TP, Mo B, Wang L, Zhang S, Wang C. 2020. Raman study of barite and celestine at various temperatures. *Minerals* 10:260. <https://doi.org/10.3390/min10030260>.
- Walsby AE, Reynolds CS. 1980. Sinking and floating, p 371–412. *In* Morris I (ed), *The physiological ecology of the phytoplankton*. Blackwell Science, Oxford, United Kingdom.

38. Knoll AH. 2003. Biomineralization and evolutionary history. *Rev Mineral Geochem* 54:329–356. <https://doi.org/10.2113/0540329>.
39. Kreger DR, Boeré H. 1969. Some observations on barium sulphate in *Spirogyra*. *Acta Bot Neerl* 18:143–151. <https://doi.org/10.1111/j.1438-8677.1969.tb00579.x>.
40. Gawryluk RMR, Del Campo J, Okamoto N, Strasser JFH, Lukeš J, Richards TA, Worden AZ, Santoro AE, Keeling PJ. 2016. Morphological identification and single-cell genomics of marine diplomemids morphological identification. *Curr Biol* 26:3053–3059. <https://doi.org/10.1016/j.cub.2016.09.013>.
41. Cavan EL, Laurenceau-Cornec EC, Bressac M, Boyd PW. 2019. Exploring the ecology of the mesopelagic biological pump. *Prog Oceanogr* 176:102125. <https://doi.org/10.1016/j.pocean.2019.102125>.
42. Fisher NS, Guillard RRL, Bankston DC. 1991. The accumulation of barium by marine phytoplankton grown in culture. *J Mar Res* 49:339–354. <https://doi.org/10.1357/002224091784995882>.
43. Brook AJ, Grime GW, Watt F. 1988. A study of barium accumulation in desmids using the Oxford scanning proton microprobe (SPM). *Nucl Instruments Methods Phys Res* 30:372–377. [https://doi.org/10.1016/0168-583X\(88\)90027-4](https://doi.org/10.1016/0168-583X(88)90027-4).
44. Sun S, Liu M, Nie X, Dong F, Hu W, Tan D, Huo T. 2018. A synergetic biomineralization strategy for immobilizing strontium during calcification of the coccolithophore *Emiliania huxleyi*. *Environ Sci Pollut Res Int* 25:22446–22454. <https://doi.org/10.1007/s11356-018-1271-4>.
45. Kirichok Y, Kravivinsky G, Clapham DE. 2004. The mitochondrial calcium uniporter is a highly selective ion channel. *Nature* 427:360–364. <https://doi.org/10.1038/nature02246>.
46. Schumaker KS, Sze H. 1986. Calcium transport into the vacuole of oat roots. Characterization of H<sup>+</sup>/Ca<sup>2+</sup> exchange activity. *J Biol Chem* 261:12172–12178. [https://doi.org/10.1016/S0021-9258\(18\)67219-9](https://doi.org/10.1016/S0021-9258(18)67219-9).
47. Docampo R, Lukeš J. 2012. Trypanosomes and the solution of a fifty years-mitochondrial calcium mystery. *Trends Parasitol* 28:31–37. <https://doi.org/10.1016/j.pt.2011.10.007>.
48. Veronis G. 1972. On properties of seawater, defined by temperature, salinity and pressure. *J Mar Res* 30:227–255.
49. Gaft ML, Bershov LV, Krasnaya AR, Yaskolko VY. 1985. Luminescence centers in anhydrite, barite, celestite and their synthesized analogs. *Phys Chem Minerals* 11:255–260. <https://doi.org/10.1007/BF00307403>.
50. Raven JA. 1985. Regulation of pH and generation of osmolarity in vascular plants: a cost-benefit analysis in relation to efficiency of use of energy, nitrogen and water. *New Phytol* 101:25–77. <https://doi.org/10.1111/j.1469-8137.1985.tb02816.x>.
51. Butenko A, Hammond M, Field MC, Ginger ML, Yurchenko V, Lukeš J. 2021. Reductionist pathways for parasitism in Euglenozoans? Expanded datasets provide new insights. *Trends Parasitol* 37:100–116. <https://doi.org/10.1016/j.pt.2020.10.001>.
52. De Vargas C, Aubry M-P, Probert I, Young J. 2007. Origin and evolution of coccolithophores: from coastal hunters to oceanic farmers, p 251–285. *Evolution of primary producers in the sea*. Elsevier, Amsterdam, Netherlands.
53. Tashyreva D, Prokopchuk G, Yabuki A, Kaur B, Faktorová D, Votýpka J, Kusaka C, Fujikura K, Shiratori T, Ishida K-I, Horák A, Lukeš J. 2018. Phylogeny and morphology of new diplomemids from Japan. *Protist* 169:158–179. <https://doi.org/10.1016/j.protis.2018.02.001>.
54. Prokopchuk G, Tashyreva D, Yabuki A, Horák A, Masařová P, Lukeš J. 2019. Morphological, ultrastructural, motility and evolutionary characterization of two new Hemistasiidae species. *Protist* 170:259–282. <https://doi.org/10.1016/j.protis.2019.04.001>.
55. Tashyreva D, Prokopchuk G, Votýpka J, Yabuki A, Horák A, Lukeš J. 2018. Life cycle, ultrastructure, and phylogeny of new diplomemids. *mBio* 9:e02447-17. <https://doi.org/10.1128/mBio.02447-17>.
56. Moudříková Š, Sadowsky A, Metzger S, Nedbal L, Mettler-Altmann T, Mojžeš P. 2017. Quantification of polyphosphate in microalgae by Raman microscopy and by a reference enzymatic assay. *Anal Chem* 89:12006–12013. <https://doi.org/10.1021/acs.analchem.7b02393>.
57. Moudříková Š, Mojžeš P, Zachleder V, Pfaff C, Behrendt D, Nedbal L. 2016. Raman and fluorescence microscopy sensing energy-transducing and energy-storing structures in microalgae. *Algal Res* 16:224–232. <https://doi.org/10.1016/j.algal.2016.03.016>.
58. Moudříková Š, Nedbal L, Solovchenko A, Mojžeš P. 2017. Raman microscopy shows that nitrogen-rich cellular inclusions in microalgae are microcrystalline guanine. *Algal Res* 23:216–222. <https://doi.org/10.1016/j.algal.2017.02.009>.
59. Barcytė D, Pilátová J, Mojžeš P, Nedbalová L. 2020. The arctic *Cylindrocapsa* (Zygnematophyceae, Streptophyta) green algae are genetically and morphologically diverse and exhibit effective accumulation of polyphosphate. *J Phycol* 56:217–232. <https://doi.org/10.1111/jpy.12931>.
60. Pilátová J, Pánek T, Oborník M, Čepička I, Mojžeš P. 2022. Revisiting biocrystallization: purine crystalline inclusions are widespread in eukaryotes. *ISME J* 16:2290–2294. <https://doi.org/10.1038/s41396-022-01264-1>.
61. Yurchenko V, Votýpka J, Tesarová M, Klepetková H, Kraeva N, Jirků M, Lukeš J. 2014. Ultrastructure and molecular phylogeny of four new species of monoxenous trypanosomatids from flies (Diptera: Brachycera) with redefinition of the genus *Wallaceina*. *Folia Parasitol* 61:97–112. <https://doi.org/10.14411/fp.2014.023>.
62. Gemmi M, Mugnaioli E, Gorelik TE, Kolb U, Palatinus L, Boullay P, Hövmöller S, Abrahams JP. 2019. 3D electron diffraction: The nanocrystallography revolution. *ACS Cent Sci* 5:1315–1329. <https://doi.org/10.1021/acscentsci.9b00394>.
63. Palatinus L, Brázda P, Jelínek M, Hrdá J, Steciuk G, Klementová M. 2019. Specifics of the data processing of precession electron diffraction tomography data and their implementation in the program PETS2.0. *Acta Crystallogr B Struct Sci Cryst Eng Mater* 75:512–522. <https://doi.org/10.1107/S2052520619007534>.
64. Petříček V, Dušek M, Palatinus L. 2014. Crystallographic computing system JANA2006: general features. *Z Krist* 229:345–352. <https://doi.org/10.1515/zkri-2014-1737>.
65. Belevich I, Joensuu M, Kumar D, Vihinen H, Jokitalo E. 2016. Microscopy Image Browser: a platform for segmentation and analysis of multidimensional datasets. *PLoS Biol* 14:e1002340. <https://doi.org/10.1371/journal.pbio.1002340>.
66. Zhao F, McGrath SP, Crosland AR. 1994. Comparison of three wet digestion methods for the determination of plant sulphur by inductively coupled plasma atomic emission spectroscopy (ICP-AES). *Commun Soil Sci Plant Anal* 25:407–418. <https://doi.org/10.1080/00103629409369047>.
67. Andresen E, Lyubenova L, Hubáček T, Bokhari SNH, Matoušková Š, Mijovilovich A, Rohovec J, Küpper H. 2020. Chronic exposure of soybean plants to nanomolar cadmium reveals specific additional high-affinity targets of cadmium toxicity. *J Exp Bot* 71:1628–1644. <https://doi.org/10.1093/jxb/erz530>.
68. Strbkova L, Carson BB, Vincent T, Vesely P, Chmelik R. 2020. Automated interpretation of time-lapse quantitative phase image by machine learning to study cellular dynamics during epithelial–mesenchymal transition. *J Biomed Opt* 25:e086502.
69. Decelle J, Not F. 2015. *Acantharia*. John Wiley & Sons, Hoboken, NJ.